

# Quasicrystalline Analogue of the Haldane Model

B. D. K. Burgess<sup>1,\*</sup> and N. R. Cooper<sup>1</sup>

<sup>1</sup>TCM Group, Cavendish Laboratory, University of Cambridge, J.J. Thomson Avenue, Cambridge, CB3 0US, United Kingdom

We present a model for a topological quasicrystalline system which is suitable for realisation in cold-atom experiments. We define the model in terms of complex momentum-space couplings which break time-reversal symmetry (TRS), and detail how it may be experimentally realised using two-photon Raman couplings. In the weak-potential limit, we study the model analytically by calculating the bandstructure over a ‘quasi-Brillouin zone’ (QBZ). We find symmetry-protected Dirac cones, which are gapped by a TRS-breaking term, resulting in a Chern number  $C = 1$ . This provides a direct analogy to the Haldane model, but now in a quasicrystalline setting. We also infer the number of states below the topological gap from the QBZ area. We verify our analysis with numerical calculations of periodic approximants to our system, constructing a phase diagram in parameter space which shows a topological region extending beyond the weak-potential regime. We also find examples of narrow Chern bands with the potential for hosting strongly-correlated physics. Our work raises questions about the nature of localisation and strongly-correlated states in Chern bands in quasiperiodic systems.

## I. INTRODUCTION

Quasicrystals are spatially ordered but not periodic [1, 2], making them a middle-ground between aperiodic and crystalline systems. In recent years, quasicrystals have been of particular interest for their unconventional localisation properties of quantum particles, which differ from those of randomly disordered systems. For random disorder, all single-particle states are Anderson-localised in one or two spatial dimensions [3–5]. Quasicrystalline systems, on the other hand, can host extended states for sufficiently weak potentials, as exemplified by the prototypical Aubry-André model [6–8]. Other quasiperiodic models in 1D and 2D possess spectra where extended and localised states coexist [9–17], or host intermediate ‘critical’ states [18, 19].

The physics becomes especially rich in the case of many-body localisation (MBL) of interacting particles [20–22]. MBL in 1D systems is well-studied theoretically for both random disorder [23–31] and quasicrystals [32–35]; the MBL transition is found to belong to a different universality class in each case [36, 37]. MBL has also been observed experimentally in both types of system [38–41]. In 2D, the physics becomes richer still, and the existence of MBL is the subject of ongoing debate. It is theorised that true MBL cannot occur for random disorder, due to rare ergodic regions which trigger an ‘avalanche of thermalisation’ [42–48]. However, there is experimental [49, 50] and theoretical [51–59] work suggesting that MBL behaviour survives, at least on finite timescales. In quasicrystals, which are deterministic, these rare regions are absent and it is theorised that MBL does occur [16, 58, 60]; this is supported by experimental results [61–63].

When the energy states of a quasicrystal can also be characterised by some topological invariant, novel effects

can occur due to the interplay between the quasiperiodicity and the topology [64, 65]. Recently, such topological quasicrystals have been widely investigated through the numerical analysis of real-space tight-binding models on quasiperiodic lattices such as the Penrose or Ammann-Beenker tilings. A great range of interesting phenomena have been reported, including unconventional ‘bulk-localised transport’ states [66–68], higher-order topological insulators [69–74], topological pumping and protected transport [75–84], and topological superconductivity [85–90]. In contrast, the existing experimental research into topological quasicrystals is limited to a small number of photonic experiments [79, 91–93].

Thus, both topological and non-topological quasicrystals are host to rare and interesting phenomena, and are currently the subject of widespread research. In this paper, we aim to increase the scope for experimental work in this area by presenting a model for a topological quasicrystal which is realisable with an optical lattice in cold atom experiments [94–96]. These experiments have the advantages of highly tunable parameters, a lack of disorder, and isolation of the system from the environment, which have enabled various landmark results in the field [40, 62, 97–101]. Optical lattices have previously been implemented to investigate both quasicrystals [7, 40, 62, 102–104] and topological systems [105–109] individually; here, we combine the two. Specifically, we adapt the ‘optical flux lattice’ (OFL) approach for generating topological optical lattices [110–112] to a quasicrystalline geometry, creating opportunities for the experimental investigation of these exotic systems. Since our model for a topological quasicrystal is naturally defined and investigated in reciprocal space, we are led to adopt different theoretical approaches to previous theoretical works considering real-space tight-binding models [66–90]. While the motivation for our work is to generate topological quasicrystals for cold atoms, we note that the periodic OFL models also naturally emerge in layered 2D materials [113, 114]. One can therefore anticipate that the quasicrystalline models we introduce here also have

\* bb611@cam.ac.uk

analogues in quasicrystalline layered materials [115].

The remainder of the paper is structured as follows. We motivate our model Hamiltonian with reference to previous work on OFLs in Sec. II; we then detail exactly how it may be experimentally realised in Sec. III. Next, we analyse the model in Secs. IV-V: we demonstrate that it is topologically non-trivial, construct the phase diagram of the system in parameter-space, and investigate the particle density required to fill all states below the topological energy gap. We summarise our work in Sec. VI.

## II. MODEL

### A. Optical Flux Lattices

We first briefly introduce OFLs in general terms, to explain how these give rise to topological bandstructures. We consider a particle with  $N$  internal states moving in 2D, with Hamiltonian:

$$H = \frac{\mathbf{p}^2}{2m} \otimes \mathbb{1}_N + V(\mathbf{r}) \quad (1)$$

where  $V(\mathbf{r})$  is an  $N \times N$  matrix coupling different spin states. In the adiabatic limit of large potential energy, the particle follows the same local spinor eigenstate  $|n(\mathbf{r})\rangle$  of  $V(\mathbf{r})$ . As it moves through space, it acquires a Berry phase due to the changing of  $|n(\mathbf{r})\rangle$  with position. By projecting  $H$  onto the spinor texture  $|n(\mathbf{r})\rangle$ , one finds an effective Hamiltonian which is that of a scalar particle moving in the background of a gauge potential [110]:

$$\mathbf{A}(\mathbf{r}) = i \langle n(\mathbf{r}) | \nabla_{\mathbf{r}} n(\mathbf{r}) \rangle \quad (2)$$

with associated ‘effective magnetic field’:

$$\mathbf{B}_{\text{eff}}(\mathbf{r}) = \nabla_{\mathbf{r}} \times [i \langle n(\mathbf{r}) | \nabla_{\mathbf{r}} n(\mathbf{r}) \rangle] \cdot \hat{\mathbf{z}}. \quad (3)$$

(We set  $\hbar = 1$ ). These are respectively the (real-space) Berry potential and Berry curvature of  $|n(\mathbf{r})\rangle$ . This emergent magnetic field explains why OFLs acquire non-trivial topological properties for a suitable form of  $V(\mathbf{r})$ .

It is also instructive to consider a reciprocal-space description of OFLs [112]. The potential energy term has Fourier components:

$$V_{\mathbf{G}, \sigma' \sigma} = \langle \mathbf{q} + \mathbf{G}, \sigma' | V(\mathbf{r}) | \mathbf{q}, \sigma \rangle, \quad (4)$$

where  $\mathbf{q}$  is the particle momentum, and  $\sigma$  indexes the spin states. Again working in the limit of zero kinetic energy, the Hamiltonian takes the form of a tight-binding model, where  $V_{\mathbf{G}, \sigma' \sigma}$  are the ‘hopping’ matrix elements between ‘sites’ in momentum space (allowed states  $|\mathbf{q}, \sigma\rangle$ ). For a set of matrix elements which give a net phase upon hopping round a closed set of transfers in momentum space, time-reversal symmetry (TRS) is broken, and the resulting OFL can be topologically non-trivial. This is analogous to the Haldane model [116], except that here it

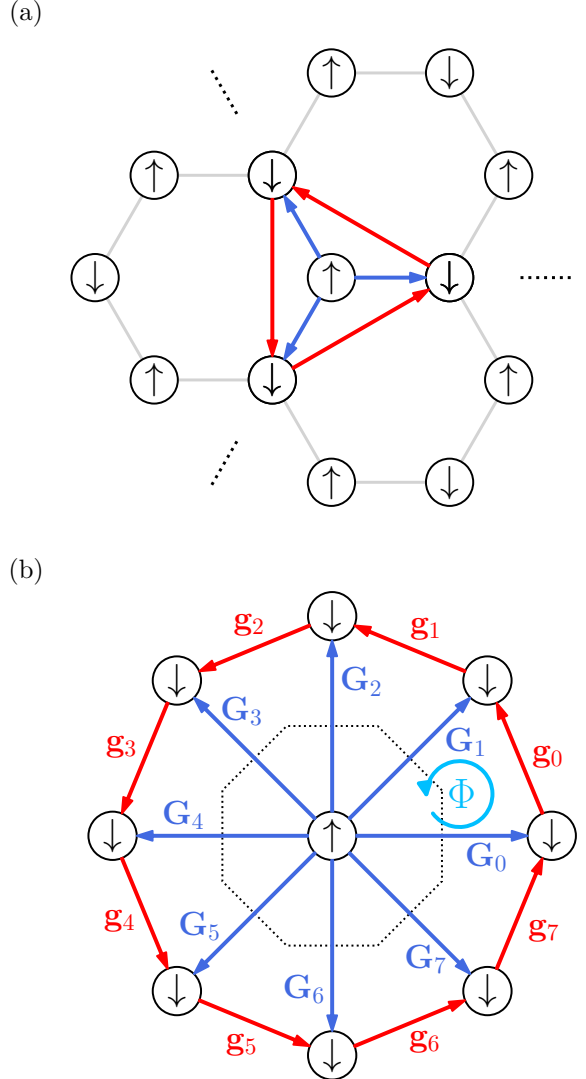


FIG. 1: Couplings in momentum space for (a) the “dual Haldane model” and (b) our quasiperiodic model. Upon hopping anticlockwise around a triangular plaquette, the atom acquires a phase  $\Phi$  from the complex coupling elements. The quasi-Brillouin zone (see Sec. IV) is shown dotted in black.

is hoppings in momentum space, rather than real-space, that are responsible for breaking TRS. It is important to note that TRS remains broken even for non-vanishing kinetic energy, so we do not actually require the strong-potential limit to realise a topological bandstructure.

### B. Reciprocal-Space Construction

We now construct the specific model that we will consider for the remainder of the paper. This is an adaptation of the “dual Haldane model” presented in [111], in which the couplings in momentum space [Fig. 1(a)] take the form of the Haldane model, with  $|\sigma = \uparrow\rangle$  and  $|\sigma = \downarrow\rangle$  states occupying the two inequivalent sites of the hon-

eycomb lattice. There, each  $|\uparrow\rangle$  site is coupled to three nearest-neighbour  $|\downarrow\rangle$  sites with 3-fold rotational symmetry, in addition to next-nearest-neighbour coupling between like spins. Here, we make a quasiperiodic lattice by coupling the  $|\uparrow\rangle$  site to eight neighbouring  $|\downarrow\rangle$  sites with 8-fold rotational symmetry, as well as retaining the couplings between like spins [Fig. 1(b)]. Our Hamiltonian takes the form:

$$H = \frac{\mathbf{p}^2}{2m} \otimes \mathbb{1}_2 + H_U + H_V \quad (5a)$$

$$H_U = \sum_{l=0}^7 U_l e^{-i\mathbf{G}_l \cdot \mathbf{r}} \otimes \sigma_+ + \text{h.c.} \quad (5b)$$

$$H_V = \sum_{l=0}^7 V_l e^{-i\mathbf{g}_l \cdot \mathbf{r}} \otimes \sigma_z + \text{h.c.} \quad (5c)$$

where  $\sigma_+ = (\sigma_x + i\sigma_y)/2$  and  $\sigma_{x,y,z}$  are the Pauli matrices.  $H_U$  generates the coupling between opposite spins, while  $H_V$  couples like spins. The Fourier components of the potential have the desired 8-fold rotational symmetry:

$$\mathbf{G}_l = |\mathbf{G}| (\cos(\pi l/4), \sin(\pi l/4))^T \quad (6a)$$

$$\mathbf{g}_l = \mathbf{G}_{l+1} - \mathbf{G}_l \quad (6b)$$

with  $l \in [0, 7]$ . (We have also analysed an analogous system with 5-fold rotational symmetry, which shows qualitatively similar results; see Appendix A). The wavelength  $\lambda = 2\pi/|\mathbf{G}|$  provides the natural lengthscale of the system. Since these  $\mathbf{G}_l$  are incommensurate with one another, the minimal rank of the basis set spanning the potential (4) exceeds the spatial dimension (2), and the system is quasicrystalline by definition [2].

Analogous to the Haldane model, we wish to choose couplings which break TRS due to the non-zero complex phase  $\Phi$  acquired upon hopping round any closed set of momentum transfers. For quasicrystals, there is an additional complication that combinations of basis vectors  $\mathbf{G} = \sum_i n_i \mathbf{G}_i$  with  $n_i \in \mathbb{Z}$  fill reciprocal space densely, instead of forming the sparse reciprocal lattice of a periodic system as in Fig. 1(a). For simplicity, we only show the ‘first-order’ couplings in Fig. 1(b); nevertheless, these are sufficient to enable us to choose  $U_l$  and  $V_l$  elements for which TRS is broken.

We choose constant  $V_l = V \forall l$  for simplicity. Since  $\mathbf{g}_l = -\mathbf{g}_{l+4}$ , the effective matrix element for a transfer by momentum  $\mathbf{g}_l$  is  $V_l^* + V_{l+4} = 2 \text{Re}[V]$ , and we can pick  $V \in \mathbb{R}$  without loss of generality. To retain the rotational symmetry and ensure that the phase is the same for each triangular plaquette in Fig. 1(b), we choose:

$$U_l = -U e^{-i\pi Rl/4} \quad (7)$$

with  $R \in \mathbb{Z}$ . When starting from a  $|\uparrow\rangle$  state, this results in a total acquired phase:

$$\Phi_\uparrow = \arg(U_l^* \cdot -2V \cdot U_{l+1}) = \text{mod}\left(-\frac{\pi R}{4}, 2\pi\right) - \pi \quad (8)$$

with the modulus operation ensuring that  $-\pi \leq \Phi_\uparrow < \pi$ . Alternatively, we could consider starting from a  $|\downarrow\rangle$  state (not depicted in Fig. 1(b)), in which case the acquired phase would be:

$$\Phi_\downarrow = \arg(U_l \cdot 2V \cdot U_{l+1}^*) = \text{mod}\left(\frac{\pi R}{4} + \pi, 2\pi\right) - \pi \quad (9)$$

Throughout this work, we take  $R = 5$ , giving  $\Phi_\uparrow = -\pi/4$  and  $\Phi_\downarrow = -3\pi/4$ ; we will find that this leads to a Chern number  $\mathcal{C} = +1$ . We emphasise that it is really  $H_V$  which breaks TRS due to its  $\sigma_z$  coupling; without this, the phases from  $H_U$  would cancel out as  $\Phi_\uparrow = -\Phi_\downarrow$ . The associated magnetic field  $B_{\text{eff}}(\mathbf{r})$  of the model inherits the quasiperiodic octagonal symmetry of the Hamiltonian [117].

### III. IMPLEMENTATION FOR COLD ATOMS

Having motivated our Hamiltonian in the previous section, we now demonstrate how it could be realised in a cold-atom experiment. Our strategy will be to use two-photon Raman transitions to generate the required momentum shifts and couplings between spin states, which in general may be any two angular momentum states. (In the 2D materials setting [113], the role of spin is provided by the layer index.) For simplicity of presentation, we consider an atomic species with a ground level with angular momentum  $1/2$ , with states denoted  $\{|g, \uparrow\rangle, |g, \downarrow\rangle\}$ , and an excited level also of angular momentum  $1/2$ , with states  $\{|e, \uparrow\rangle, |e, \downarrow\rangle\}$ . Possible atomic species include  $^{171}\text{Yb}$  or  $^{199}\text{Hg}$  [111]. We imagine that the spin-degeneracy is lifted, for example due to the Zeeman shift from an applied magnetic field, resulting in splitting of both the ground and excited levels by an energy  $\delta$ .

We characterise our lasers by complex electric field amplitudes  $\boldsymbol{\epsilon} \in \mathbb{C}^3$ , such that the physical electric field is  $\mathbf{E}(\mathbf{r}, t) = \text{Re}[\boldsymbol{\epsilon} e^{i(\mathbf{k} \cdot \mathbf{r} - \omega t)}]$ . For a two-photon process involving absorption from laser  $i$  and emission into laser  $j$ , the resulting potential energy term is given by [118]:

$$V(\mathbf{r}) \propto \left( \frac{\boldsymbol{\epsilon}_i^* \times \boldsymbol{\epsilon}_j}{\Delta} \cdot \boldsymbol{\sigma} \right) e^{i\Delta\mathbf{k} \cdot \mathbf{r}} \quad (10)$$

where  $\Delta\mathbf{k} = \mathbf{k}_i - \mathbf{k}_j$  is the momentum kick acquired from the two photons,  $\boldsymbol{\sigma} = (\sigma_x, \sigma_y, \sigma_z)^T$  is the vector of Pauli spin matrices and  $\Delta$  is the detuning of the transition energy from the excited state (taken to be large enough that any population of the excited state can be neglected). We build up our desired potential [Eq. (5)] term-by-term by adding pairs of lasers to our setup.

The full diagram of lasers and the corresponding atomic energy transitions are shown in Fig. 2. To generate the  $H_U$  terms, we couple lasers with wavevectors  $\mathbf{G}_l$  and  $\boldsymbol{\epsilon}_l^G$  linearly polarised along  $z$ , to lasers propagating along  $z$  with  $\boldsymbol{\epsilon}_l^{\sigma+}$  circularly polarised in the  $xy$ -plane. Taking the  $z$  momentum kick to be suppressed by an external trapping potential, this generates the required

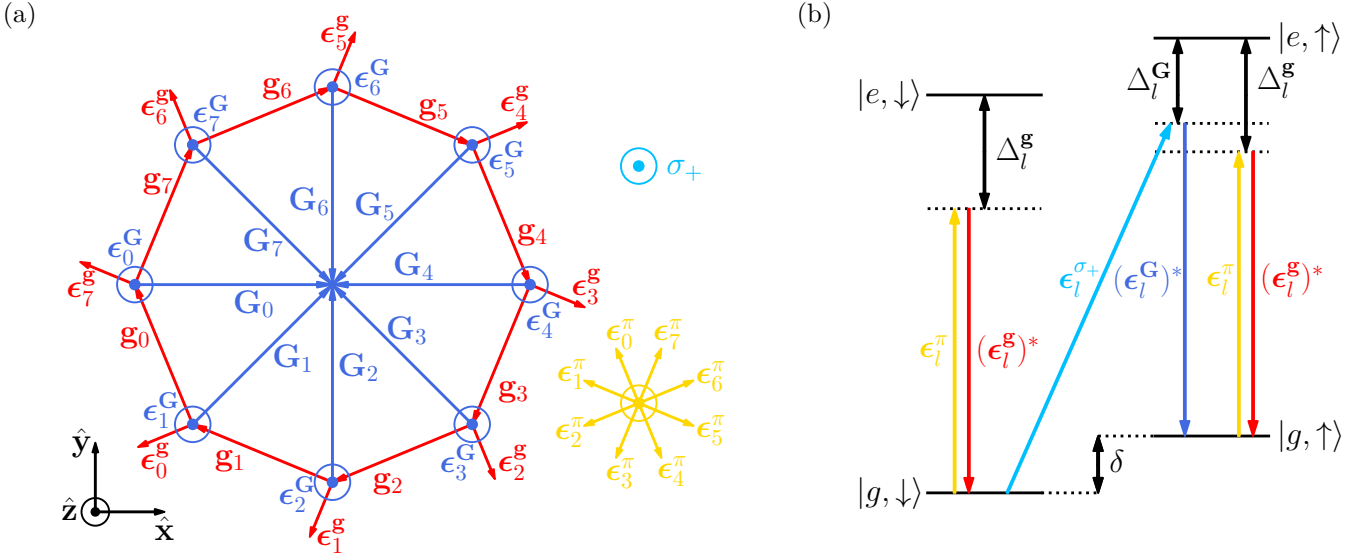


FIG. 2: (a) Laser wavevectors and electric field directions. The  $\epsilon_l^{\sigma+}$  (light blue) and  $\epsilon_l^{\pi}$  (yellow) lasers propagate in the  $z$ -direction, out of the plane. The circularly-polarised  $\epsilon_l^{\sigma+}$  electric fields (not depicted) rotate in the  $xy$ -plane; all other lasers are linearly polarised along the directions indicated. (b) Illustration of the energy levels and transitions contributing to the Hamiltonian. The coloured arrows indicate absorption or emission of a photon from the corresponding laser in (a). The  $\epsilon_l^{\sigma+}/\epsilon_l^G$  (light/dark blue) process generates the  $H_U$  terms, and the  $\epsilon_l^{\pi}/\epsilon_l^g$  (yellow/red) process generates the  $H_V$  terms.

momentum components  $e^{-i\mathbf{G}_l \cdot \mathbf{r}}$ , and the electric field directions give the required  $\sigma_+$  coupling in spin-space. The associated amplitude is:

$$U_l \propto \frac{|(\epsilon_l^G)^* \times \epsilon_l^{\sigma+}|}{\Delta_l^G}. \quad (11)$$

Similarly for the  $H_V$  terms, we couple between lasers with wavevectors  $\mathbf{g}_l$  and  $z$ -propagating lasers, this time with  $\epsilon_l^g$  and  $\epsilon_l^{\pi}$  both linearly polarised in the  $xy$ -plane, but orthogonal to each other. This gives the required momentum components  $e^{-i\mathbf{g}_l \cdot \mathbf{r}}$  and  $\sigma_z$  coupling, with amplitudes:

$$V_l \propto \frac{|(\epsilon_l^g)^* \times \epsilon_l^{\pi}|}{\Delta_l^g}. \quad (12)$$

This scheme allows us to choose any  $U_l, V_l \in \mathbb{C}$  by adjusting the laser amplitudes, detunings and relative phases.

We imagine choosing different detunings  $\Delta_l^{\mathbf{G}/\mathbf{g}}$ , so all lasers are incoherent except for the 16 pairs generating the matrix elements  $U_l$  and  $V_l$ . This realises exactly our Hamiltonian Eq. (5), but may be challenging experimentally. An alternative scheme is outlined in Appendix B, which requires only five lasers, all of which are coherent. This comes at the cost of making  $U_l$  and  $V_l$  dependent on one another, and introducing additional momentum couplings into the Hamiltonian. We have analysed both cases and find similar qualitative behaviour, but we will focus on the first scheme for maximum clarity.

#### IV. PLANE-WAVE ANALYSIS

##### A. Quasi-Brillouin Zone

We now analyse our model to demonstrate that it does possess the desired non-trivial topological properties. To provide analytic insight, we first consider the system in the ‘nearly-free’ limit of weak potential applied in Refs. [119, 120]. We shall later show that the (topological) features derived within this analytic approach survive also to deeper lattice depths.

For  $U = V = 0$ , the energy eigenstates of the system are simply the plane-wave states  $|\mathbf{q}, \sigma\rangle$ , with  $\sigma \in \{\uparrow, \downarrow\}$  as before. The energy levels form the (spin-degenerate) parabola  $E(\mathbf{q}) = |\mathbf{q}|^2/2m$ . We first introduce  $H_U$  only, with a small  $U \ll E_R$ , where  $E_R = |\mathbf{G}|^2/2m$  is the recoil energy which sets the kinetic energy scale of the system. This couples each state  $|\mathbf{q}, \sigma\rangle$  to other states  $|\mathbf{q} - \mathbf{G}_l, \sigma'\rangle$  (with  $\sigma'$  opposite to  $\sigma$ ). This opens gaps in the parabola at first-order in  $U$  when the states have equal kinetic energy. Such states lie along the perpendicular bisectors of the  $\mathbf{G}_l$  vectors, so we generate gaps around an octagonal ‘quasi-Brillouin zone’ (QBZ), depicted in Fig. 1(b). The low-energy states with momenta inside the QBZ therefore form a region that, as we show below, can be separated by a gap from the other states to form a topological band.

Just as the Brillouin zone area (in reciprocal space) determines the number of states in a band in a periodic system, the QBZ area determines the number of states in our band here. Imposing periodic boundary conditions over an arbitrary area  $L^2$ , allowed states occupy an area  $(2\pi/L)^2$  in reciprocal space, so the required atomic

density to fill all the states is calculated geometrically to be:

$$n = \frac{2A_{\text{QBZ}}}{(2\pi)^2} = \frac{4(\sqrt{2}-1)}{\lambda^2} \approx \frac{1.6568\ldots}{\lambda^2} \quad (13)$$

with the extra factor of 2 due to spin. We further verify this result in Sec. V C.

We pause to note that this momentum space approach gives a useful alternative perspective on the model of Ref. [17]. That work studies a similar 8-fold rotationally symmetric quasicrystal with a real-space methodology, numerically finding a (non-topological) isolated lowest band. With our methodology, we can physically understand the emergence of this isolated band due to the opening of gaps along the QBZ boundary of that system. After accounting for spin, and inserting the appropriate units of lengths, our expression for the atomic density to fill the band [Eq. (13)] agrees with that calculated by an alternative method in Ref. [17].

## B. Symmetry and Topological Properties

Having identified this isolated set of states, it is natural to investigate whether they can form a band that is topologically non-trivial. To do so, we compute the band-structure over the QBZ in the minimal basis of plane-wave states which captures all first-order couplings of the Hamiltonian. This requires 16 basis states, which are degenerate and coupled together at the QBZ corners. Explicitly, the required states  $|\mathbf{q}_i, \sigma\rangle$  are related by  $\mathbf{q}_{i+3(\text{mod } 8)} = \mathbf{q}_i - \mathbf{G}_i$ . The couplings are illustrated in Fig. 3. Diagonalising the  $16 \times 16$  Hamiltonian, we find the bandstructure in Fig. 4.

There is an additional subtlety here related to the counting of states. This is most easily appreciated by considering the  $U = 0$  system, whose eigenspectrum is simply the (spin-degenerate) free-particle parabola. Other bands should be discarded; otherwise one will overcount states at a given energy, giving an increase in the density of states above the expected constant value for a free particle in 2D. More generally, at non-zero  $U$  we should select the eigenvalues (highlighted in yellow in Fig. 4(a)) which tend to the free-particle dispersion in the limit of  $U \rightarrow 0$ .

As expected, along the QBZ boundary, we generally find a gap between the relevant bands. The exception is at the corners K, where symmetries of  $H_U$  enforce a four-fold degeneracy of states; this symmetry analysis is presented in Appendix C. In the vicinity of the corners [Fig. 4(b)], the dispersion is linear; in other words, we have two coincident Dirac cones in the bandstructure. Thus, the potential  $H_U$  leads to a semimetallic quasicrystalline system, with a density of states that vanishes linearly in energy, at least within this weak potential limit.

This semimetallic quasicrystalline state is analogous to the graphene bandstructure on which the Haldane model is built. Like in that system, we can consider adding

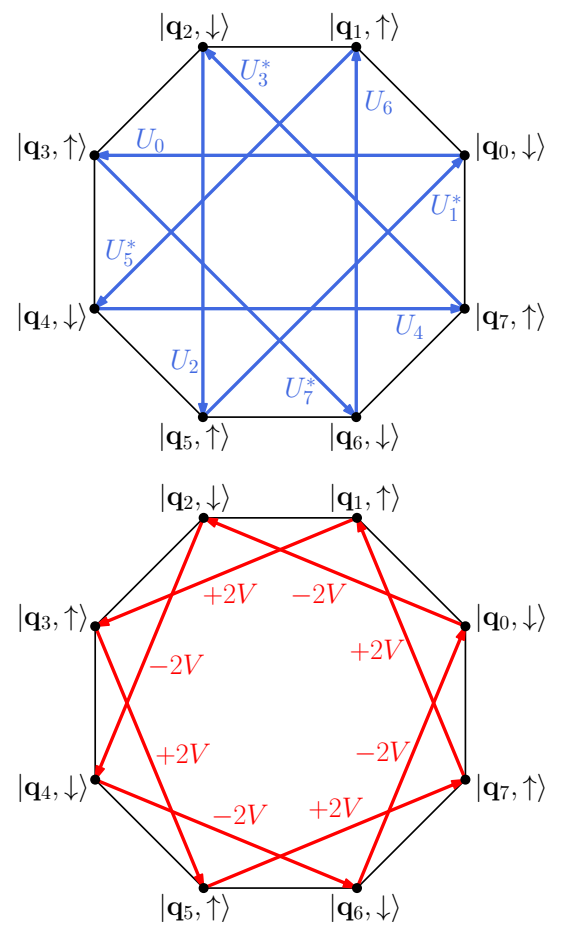


FIG. 3: Couplings of corners in the QBZ. The  $H_U$  and  $H_V$  couplings are shown on different diagrams (a) and (b) for clarity. The set of 8 states with opposite spin to those indicated here are coupled by different  $U_l$  and  $V_l$  terms; there is no coupling between the two sets.

terms to our Hamiltonian which break symmetries and open a gap at the Dirac point of this quasicrystalline lattice. A gapped Dirac cone is generically associated with a Berry flux of  $\pm\pi$ ; the topological character of the states below the gap therefore depends on whether we have the same or opposite sign of flux for each Dirac cone, corresponding to Chern number  $|\mathcal{C}| = 1$  or 0 respectively. This in turn depends on whether the perturbation breaks or preserves TRS.

One possible perturbation is  $H_V$  [Eq. (5c)], which breaks TRS by design. For our choice  $R = 5$  and  $V > 0$ , both bands below the gap contribute a Berry flux of  $+\pi$ , resulting in  $\mathcal{C} = 1$ . This demonstrates that our model Hamiltonian Eq. (5) does indeed describe a topological quasicrystal. To illustrate that TRS-preserving perturbations are also possible, we consider:

$$H_W = W \sum_{l=0}^7 (-1)^l e^{-i\mathbf{G}_l \cdot \mathbf{r}} \otimes \mathbb{1}_2 + \text{h.c.} \quad (14)$$

with  $W \in \mathbb{R}$ . This breaks the 8-fold rotational symmetry

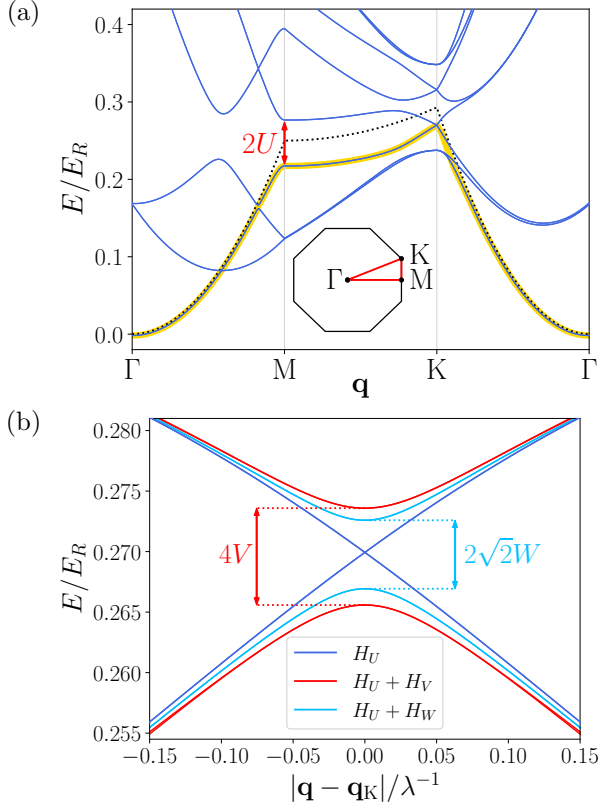


FIG. 4: (a) Bandstructure across the QBZ, calculated in the basis of the 16 plane-wave states degenerate at the K point, for  $U/E_R = 0.03$ ,  $V = W = 0$ . The path in the QBZ is shown inset. All bands here are doubly degenerate. The relevant states are those highlighted in yellow which tend to the free-particle dispersion (black dotted curve) as  $U \rightarrow 0$ . (b) Bandstructure in the vicinity of the K point, along the line  $\Gamma$ K. The bands are calculated for  $H_U$  only (dark blue),  $H_U + H_V$  with  $V/E_R = 0.002$  (red), and  $H_U + H_W$  with  $W/E_R = 0.002$  (light blue).

and gaps the Dirac points, but does not break TRS, so the bands below the gap have opposite signs of Berry curvature and the system is topologically trivial. When projecting to the degenerate subspace at the Dirac point, we find an effective coupling strength of  $2V$  for  $H_V$ , and  $\sqrt{2}W$  for  $H_W$ , giving rise to the different gaps in Fig. 4(b). In general, when both  $V$  and  $W$  are non-zero, the Chern number is simply determined by whichever term dominates:

$$\mathcal{C} = \begin{cases} 1 & \sqrt{2}V > W, \\ 0 & W > \sqrt{2}V. \end{cases} \quad (15)$$

It is important to note that since  $\mathcal{C}$  is a topological invariant, it cannot change as long as the relevant energy gap does not close. As such, although we have used the weak-coupling limit to derive the value  $\mathcal{C} = 1$ , the topological behaviour can be expected to persist as  $U$  and  $V$  increase to stronger coupling strengths.

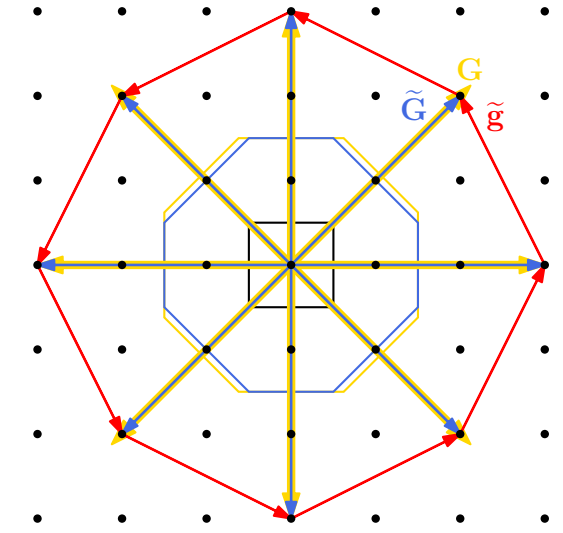


FIG. 5: Illustration of the construction of the approximant vectors, for  $N_a = 3$ . The exact quasicrystal  $\mathbf{G}_l$  are shown in yellow, and the approximant  $\tilde{\mathbf{G}}_l$  and  $\tilde{\mathbf{g}}_l$  in blue and red respectively. The approximant BZ is the black square centred on the origin; the approximant QBZ is the blue (irregular) octagon; and the quasicrystal QBZ is the yellow (regular) octagon.

## V. APPROXIMANT ANALYSIS

### A. Methodology

To confirm our analytical plane-wave results and move beyond the weak-coupling limit, we numerically analyse approximant systems. These approximate the quasicrystalline geometry, but are in fact periodic over long length-scales, and can therefore be investigated using standard techniques. We define a square lattice in reciprocal space with spacing  $|\mathbf{G}|/N_a$ , with  $N_a \in \mathbb{N}$ . The approximant  $\mathbf{G}$ -vectors  $\tilde{\mathbf{G}}_l$  are then found by ‘rounding’ the quasicrystalline  $\mathbf{G}_l$  to the nearest lattice point, thereby becoming commensurate with each other (see Fig. 5). The approximant  $\tilde{\mathbf{g}}_l$  are given by  $\tilde{\mathbf{G}}_{l+1} - \tilde{\mathbf{G}}_l$  as before. The approximant Hamiltonian  $\tilde{H}$  has identical form to Eq. (5), but with  $\tilde{\mathbf{G}}_l$  and  $\tilde{\mathbf{g}}_l$  substituted for  $\mathbf{G}_l$  and  $\mathbf{g}_l$ . As all basis vectors are commensurate,  $\tilde{H}$  is periodic. The Brillouin zone (BZ) of the approximant model is the square region (in reciprocal space)  $-\frac{|\mathbf{G}|}{2N_a} < q_x, q_y < \frac{|\mathbf{G}|}{2N_a}$ , and the real space lattice constant is  $a = N_a \lambda$ . The quasicrystal corresponds to the limit  $N_a \rightarrow \infty$  where the unit cell diverges.

### B. Numerical Results

Setting  $N_a = 3$ , we obtain the approximant bandstructure [see example in Fig. 6(a)] by numerically diagonal-

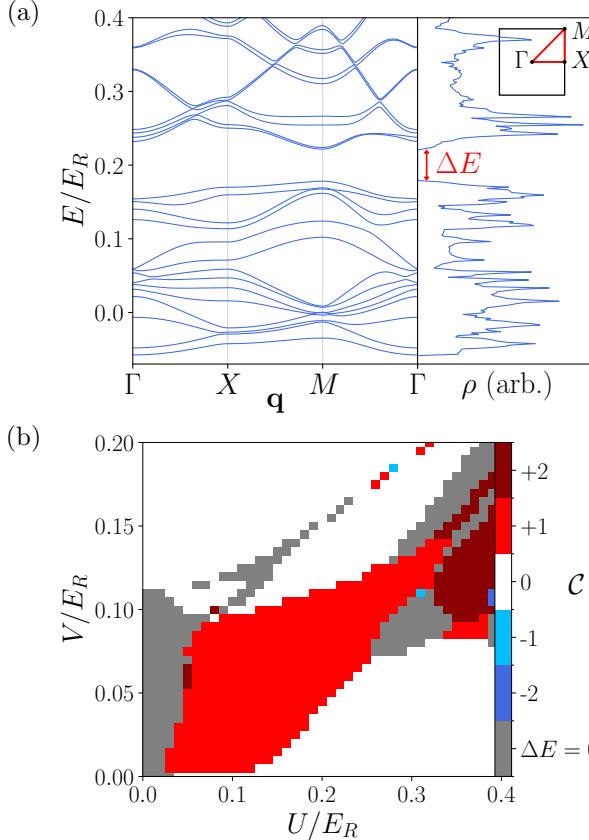


FIG. 6: (a) Example calculated bandstructure and density of states for the  $N_a = 3$  approximant system, for  $U/E_R = 0.06$  and  $V/E_R = 0.02$ . The path in the BZ is shown inset, and the energy gap  $\Delta E$  is labelled. (b) Phase diagram showing the Chern number of the bands below the energy gap, for different coupling magnitudes. At grey points, the band gap vanishes and the Chern number is not well-defined.

ising the Bloch Hamiltonian  $\tilde{H}_{\mathbf{q}} = e^{i\mathbf{q}\cdot\mathbf{r}}\tilde{H}e^{-i\mathbf{q}\cdot\mathbf{r}}$  for a set of points  $\{\mathbf{q}\}$  in the BZ. We find an energy gap  $\Delta E$  in the density of states, as predicted from the QBZ analysis. We compute the Berry curvature and Chern number summed over all the bands below the energy gap following the methodology of [121]. Repeating this for different coupling strengths  $U$  and  $V$ , we construct the phase diagram of the system in parameter space [Fig. 6(b)]. This displays a large topological region with  $C = 1$ , confirming our analysis in Sec. IV, and also demonstrating that the topological properties persist beyond the weak-coupling limit. In Appendix D, by investigating the variation of  $\Delta E$  and the size of the topological region in parameter space for increasingly accurate approximants (larger  $N_a$ ), we show that these topological properties will be preserved in the quasicrystalline limit  $N_a \rightarrow \infty$ .

As Fig. 6(b) shows, for certain coupling strengths the set of bands can attain Chern numbers other than 1 or 0. However, at these coupling strengths, the energy gap is generally small in magnitude ( $\Delta E/E_R \lesssim 0.01$ ), so we cannot be confident that these features will persist from the approximant system to the exact quasicrystal.

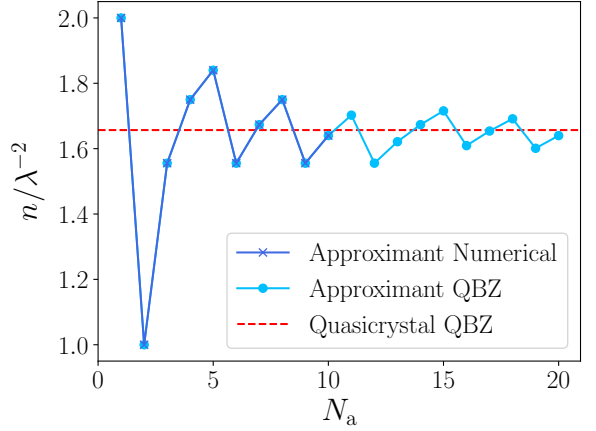


FIG. 7: Filling density for increasingly accurate approximants. The quasicrystal value calculated from the QBZ area in Eq. (13) is shown dashed in red. Dark blue points are calculated from Eq. (16) using the numerically obtained values of  $N_B$ , while light blue points are calculated from Eq. (13) using the approximant QBZ areas, and agree exactly where numerical results are available. For  $N_a > 10$ , the full numerical calculations were too expensive to perform; however, our QBZ method can still be applied, and gives results approaching the quasicrystal value as  $N_a$  increases further.

### C. Filling Density

We now compare the prediction for the atomic density to fill all states below the gap [Eq. (13)] to the numerical approximant results. These are calculated as:

$$n = \frac{N_B A_{\text{BZ}}}{(2\pi)^2} \quad (16)$$

where  $A_{\text{BZ}} = (|\mathbf{G}|/N_a)^2$  is the BZ area for the approximant  $N_a$ , and  $N_B$  is the observed number of bands below the gap in the numerically calculated bandstructures. The two bands over the QBZ have been backfolded into these  $N_B$  bands over the BZ, preserving the total number of states below the gap. The densities from Eq. (16) are expected to tend to the quasicrystalline value in the limit  $N_a \rightarrow \infty$ .

Alternatively, for each approximant we can define its own QBZ formed from the intersection of bisectors of the  $\tilde{\mathbf{G}}$ -vectors (see Fig. 5). This is an irregular octagon, unlike the regular octagon of the exact quasicrystal. Using the approximant QBZ area  $\tilde{A}_{\text{QBZ}}$  in place of  $A_{\text{QBZ}}$  in Eq. (13), we expect densities to precisely match the numerical values from Eq. (16) for all  $N_a$ . The results are plotted in Fig. 7, and show exact agreement.

### D. Narrow Chern Bands

Our numerical calculations also reveal the potential for realising narrow Chern bands, whose bandwidth  $\delta$  is much less than their gap to other topological bands  $\Delta E$ .

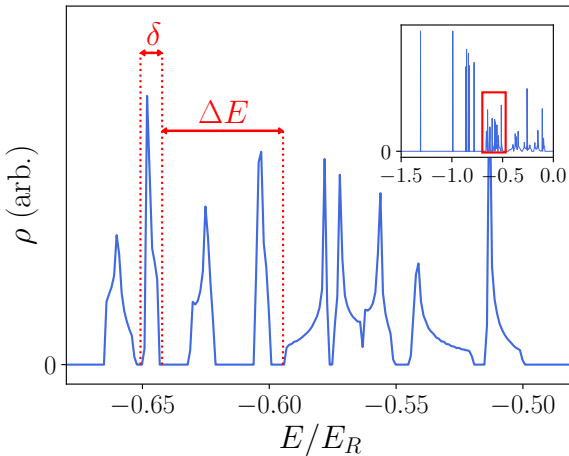


FIG. 8: Density of states for an approximant system with  $U/E_R = 0.3, V/E_R = 0.12$ . The band with width  $\delta$  is topological with  $\mathcal{C} = 1$ . The nearest topologically non-trivial band (with  $\mathcal{C} = -1$ ) is separated by the indicated energy  $\Delta E$ . The inset shows the density of states over a wider range of  $E$ ; the main plot is the region within the red box. The bands at lower energies are all topologically trivial and irrelevant for our considerations here.

(Non-topological bands can be filled and mixed with the topological band without affecting the net properties, so can be ignored). This could enable strongly-correlated phenomena to be realised in these systems, since interaction effects will dominate over kinetic energy, but not close the band gap. One such example is shown in Fig. 8, with a ratio  $\delta/\Delta E \approx 0.089$ .

The ratio  $\delta/\Delta E$  could be further decreased by thoroughly searching for optimal values of  $U$  and  $V$  in parameter-space, or adding scalar potential terms with the aim of reducing the Hamiltonian to Aharonov-Casher (AC) form following Ref. [114]. We have not yet performed any investigations along these lines, but simply note here these possible avenues for future work.

We have attempted to generalise the ‘dark state’ model discussed in Refs. [114] and [122] to a quasicrystalline geometry. As this model exactly takes on AC form for a suitable choice of laser phases and in the infinite-potential limit, it seems to be a promising candidate for realising narrow topological bands in a quasicrystalline system. However, without commensurate basis vectors, we find that the magnetic field  $B_{\text{eff}}(\mathbf{r})$  averages to zero, so the AC description is not applicable.

## VI. SUMMARY AND OUTLOOK

We have presented a model for a topological quasicrystalline system that is defined in terms of its momentum-space structure. We have shown how this model could be realised in a cold-atom experiment using two-photon Raman couplings, though similar models may arise in layered 2D electronic materials. Our model is naturally

analysed in reciprocal space by considering couplings between plane wave states. Following this methodology, in the weak-coupling limit we have shown analytically on symmetry grounds that the states within the QBZ form an isolated low-energy band with Chern number  $\mathcal{C} = 1$ . This analysis is closely analogous to that of the Haldane model – a semimetallic state converting to a topological band under the breaking of time-reversal symmetry – but now in a quasicrystalline lattice. We have confirmed our analysis with numerical calculations of periodic approximants to the quasicrystal, finding a topological phase with  $\mathcal{C} = 1$  which persists over a large region in parameter space, and verifying that the number of states below the topological gap corresponds to the QBZ area. We have also found relatively narrow Chern bands for certain choices of parameters, raising the possibility of realising strongly-correlated phases in these systems, if these bands could be flattened further.

Our work raises questions about the nature of Chern bands in quasicrystalline systems. One such question relates to the localisation of states. As detailed in Sec. I, localisation phenomena in non-topological quasicrystals are already the subject of considerable interest; similarly, the behaviour of a (topological) Landau level in the presence of random disorder has been extensively studied [123] and continues to attract attention [124–127]. The case here of localisation in a topological quasicrystalline system may display even richer physics. A second question relates to the nature of strongly-correlated phases when particles within a (nearly) flat band interact. Here, due to the quasicrystalline Hamiltonian, we expect a non-uniform and quasicrystalline particle density, which in turn controls the interactions in the system. This could result in fundamentally different behaviour to the familiar fractional quantum Hall or fractional Chern insulator states, which have uniform and periodic particle densities respectively. Investigating these questions in detail is beyond the scope of this paper, but we note them as potential avenues for future work.

## ACKNOWLEDGMENTS

We thank U. Schneider and Y. Yang for helpful discussions. This work was supported by the EPSRC [grant numbers EP/V062654/1 and EP/Y01510X/1] and a Simons Investigator Award [Grant No. 511029].

## DATA AVAILABILITY

The data and code supporting the findings of this article are openly available [128].

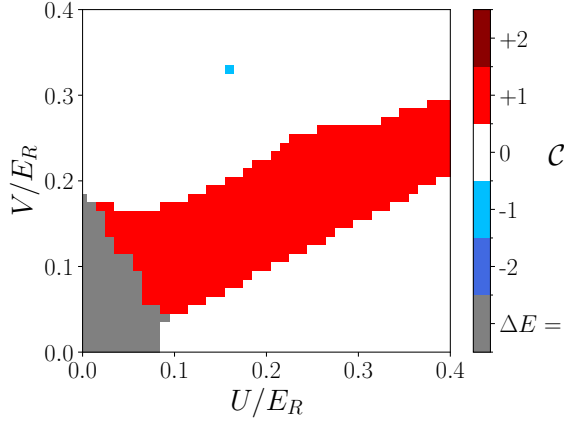


FIG. 9: Phase diagram of the 5-fold rotationally symmetric system, calculated for the  $N_a = 4$  approximant.

### Appendix A: Pentagonal System

We have performed the same analysis for an analogous system with 5-fold rotational symmetry. Here, the basis vectors are given by:

$$\mathbf{G}_l = |\mathbf{G}| (\cos(2\pi l/5), \sin(2\pi l/5))^T \quad (\text{A1a})$$

$$\mathbf{g}_l = \mathbf{G}_{l+1} - \mathbf{G}_l \quad (\text{A1b})$$

with  $l \in [0, 4]$ . We take  $V_l = V \in \mathbb{R}$  as before, and  $U$ -couplings:

$$U_l = -U e^{-2\pi i R l/5} \quad (\text{A2})$$

now with  $R = 3$ . Unlike the previous 8-fold symmetric system, this 5-fold system does not possess symmetry-protected Dirac points at the corners of its (pentagonal) QBZ for  $V = 0$ ; instead, it is gapped everywhere along the QBZ boundary by the  $U$ -couplings. Additionally, the required  $U$  to achieve a full spectral gap across the QBZ is larger than for the 8-fold system (due to the larger kinetic energy difference between the M and K points here). These factors mean that our plane-wave methodology cannot reliably be applied, since we will violate the requirement  $U, V \ll E_R$ . Instead, we simply analyse the system using periodic approximants. The phase diagram [Fig. 9] shows that the system becomes topological for  $V \sim U$ , which is as expected;  $V$  must increase until it can close and reopen the non-topological  $U$ -coupling gap. These calculations also confirm the inapplicability of the plane-wave methodology by explicitly showing that the system is gapless when  $U, V \ll E_R$ . However, interestingly, we have found that the QBZ still accurately predicts the number of states below the gap in the topological phase.

### Appendix B: Coherent Scheme

As discussed in the main text, achieving 16 pairs of coherent lasers will pose a significant experimental chal-

lengue. Here, we present an alternative scheme requiring only 5 coherent lasers, which may be more realistic in practice. In this alternative scheme, we will choose all lasers to be coherent with each other. As before, we require in-plane lasers with wavevectors  $\mathbf{G}_l$ , although using reflections means that only four separate lasers are required. Two-photon processes coupling between these lasers will generate all required  $H_V$  terms at momenta  $\mathbf{g}_l$ , provided the electric field vectors  $\epsilon_l^G$  are chosen not directly along  $z$ , but with some component in the  $xy$ -plane. Then, we introduce one additional laser with  $\sigma_+$  polarisation propagating in the  $z$  direction. Two-photon processes between this laser and the in-plane lasers generate the  $H_U$  terms.

As indicated in the main text, this scheme comes with two additional complexities: the matrix elements  $U_l$  and  $V_l$  become dependent on each other, and we get additional couplings between different momentum states, namely at momentum transfers  $\mathbf{G}_{l+2} - \mathbf{G}_l$  and  $\mathbf{G}_{l+3} - \mathbf{G}_l$ . We have analysed this scheme for approximant systems, and still find the same qualitative conclusions: for an extended region of parameter space, the system is a Chern insulator with  $\mathcal{C} = 1$ .

### Appendix C: Symmetry Analysis

#### 1. Symmetries of $H_U$

Analysis using group theory of the symmetry operations which commute with the Hamiltonian enable the degeneracies of eigenvalues at different points in the QBZ to be determined. We first analyse  $H_U$ . One symmetry of  $H_U$  is the unitary operation:

$$\tilde{C}_8 = C_8 \otimes \exp(i \Delta\phi \sigma_z/2) \quad (\text{C1})$$

where  $C_8$  is an 8-fold spatial rotation in the 2D plane about the origin (see Fig. 10), and  $\Delta\phi = \arg(U_{l+1}/U_l) = -2\pi R/8$  is the phase shift between successive  $U_l$  matrix elements. A second unitary symmetry is:

$$\tilde{\sigma}_d = \sigma_d \otimes \sigma_y \quad (\text{C2})$$

where  $\sigma_d$  is the mirror plane indicated in Fig. 10. Combinations of these operations  $\tilde{C}_8^n$  and  $\tilde{C}_8^n \tilde{\sigma}_d$  are also symmetries. A final symmetry is the anti-unitary time-reversal symmetry:

$$\mathcal{T}_x = \mathbb{1}_r \otimes \sigma_x \mathcal{K} \quad (\text{C3})$$

where  $\mathcal{K}$  denotes complex conjugation. Note that  $\mathcal{T}_x^2 = +\mathbb{1}$ , which means we do not get any Kramers-type doubling of degeneracies.

We focus on the K point (corner) of the QBZ, and aim to demonstrate that the four-fold degeneracy at the Dirac point is symmetry-protected, rather than accidental. First, we note that the full set of 16 basis states separates into two independent sets of 8 basis states which

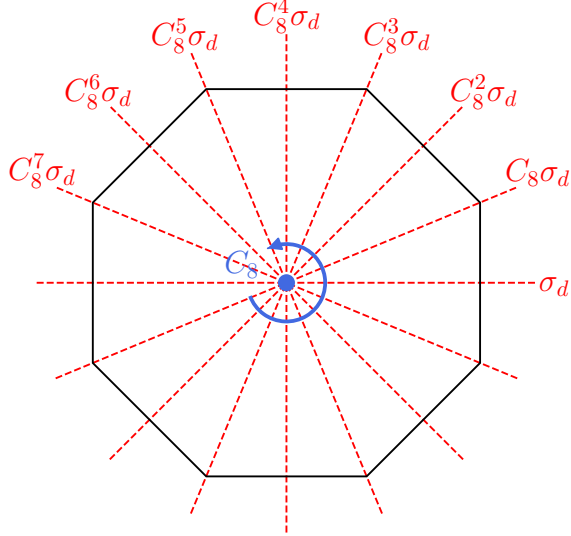


FIG. 10: Spatial symmetry operations in the QBZ: an 8-fold rotation axis (blue) and mirror planes (dashed red). The mirror operations can be expressed as combinations of a single mirror plane  $\sigma_d$  with powers of the rotation  $C_8$ .

are not coupled together. The Hamiltonian can therefore be written in block diagonal form:

$$H = \begin{pmatrix} H_1 & 0 \\ 0 & H_2 \end{pmatrix} \quad (C4)$$

with  $H_1$  and  $H_2$   $8 \times 8$  matrices in bases  $\{|\mathbf{q}_0, \uparrow\rangle, |\mathbf{q}_1, \downarrow\rangle, \dots\}$  and  $\{|\mathbf{q}_0, \downarrow\rangle, |\mathbf{q}_1, \uparrow\rangle, \dots\}$  respectively. We first consider  $H_1$  on its own.  $\tilde{C}_8$  takes  $\mathbf{q}_i \rightarrow \mathbf{q}_{i+1}$  but leaves spin unchanged; however, the basis set for  $H_1$  only contains opposite spin states between successive  $\mathbf{q}_i$ . As such, the only rotational symmetries of  $H_1$  are  $\tilde{C}_8^{2n} = \tilde{C}_4^n$ . The mirror operations  $\tilde{\sigma}_d$  and  $\tilde{C}_4^n \tilde{\sigma}_d$  remain symmetries, as they interchange momentum states but also flip the spin.

$\tilde{C}_4$  and  $\tilde{\sigma}_d$  obey the relations:

$$\tilde{\sigma}_d \tilde{C}_4 \tilde{\sigma}_d = (\tilde{C}_4)^{-1} \quad (C5a)$$

$$\tilde{C}_4^8 = \mathbb{1} \quad (C5b)$$

$$\tilde{\sigma}_d^2 = \mathbb{1} \quad (C5c)$$

and are therefore generators of  $D_8$ , the group of symmetries of an octagon. (Note that since  $R$  is odd, we have  $4\Delta\phi = \pi \pmod{2\pi}$ , and therefore  $\tilde{C}_4^4 = -\mathbb{1}$ , not simply  $\mathbb{1}$  as might naively be expected). We can explicitly construct a representation for the symmetry operations as  $8 \times 8$  matrices which commute with  $H_1$ . This representation decomposes into irreducible representations  $2E_1 \oplus 2E_3$ . Since these are all two-dimensional, all eigenvalues of  $H_1$  are doubly degenerate.

We now show that  $H_1$  and  $H_2$  have identical eigen-spectra, and therefore all eigenvalues of  $H_U$  are four-fold degenerate at the K point. We can show that  $H_U$  anti-commutes with spatial inversion  $P$ , that is  $PH_U P = -H_U$ , which relies on having  $R$  odd so that  $U_{l+4} = -U_l$ . This means that the spectrum of  $H_U$  is symmetric about 0; if  $\mathbf{v}$  is an eigenvector with eigenvalue  $\lambda$ , then  $P\mathbf{v}$  is an eigenvector with eigenvalue  $-\lambda$ . Moreover, since  $H_1$  is Hermitian, all eigenvalues are real, so taking the complex conjugate of the equation  $H_1 \mathbf{v} = \lambda \mathbf{v}$  gives that  $\mathbf{v}^*$  is an eigenvector of  $H_1^*$  with eigenvalue  $\lambda$ . By construction (that is, the choice of bases),  $H_2 = -H_1^*$ , and so the two prior results imply that  $P\mathbf{v}^*$  is an eigenvector of  $-H_1^* = H_2$  with eigenvalue  $\lambda$ . Therefore, all eigenvalues of  $H_1$  have a degenerate partner in  $H_2$ , doubling the degeneracy of the  $H_1$  eigenvalues. This proves that the coincident Dirac point we find in the bandstructure of  $H_U$  is truly protected by the symmetries of the system, rather than being accidental. We note that similar symmetry-protected Dirac points are also found in quasicrystalline  $30^\circ$  twisted bilayer graphene [129–132].

## 2. Symmetries of $H_V$

When  $H_V$  is included, we still do not introduce any coupling between the blocks  $H_1$  and  $H_2$ .  $H_V$  commutes with all of the rotational  $\tilde{C}_8$  symmetries, but breaks the mirror  $\tilde{\sigma}_d$  symmetries. This means that the group of symmetry operations of  $H_1$  is reduced from  $D_8$  down to  $C_8$ , the cyclic group of order 8. Since the cyclic group is abelian, it only has one-dimensional irreducible representations, and therefore  $H_1$  has non-degenerate eigenvalues in general. As before,  $H_1$  and  $H_2$  have identical spectra, so all eigenvalues of the full  $H$  are doubly-degenerate; however, the 4-fold degeneracy at the Dirac point is lifted, creating a gap. As discussed in the main text,  $H_V$  also breaks TRS (does not commute with  $\mathcal{T}_x$ ), so the bands below the gap can acquire a non-zero Chern number.

## 3. Symmetries of $H_W$

$H_W$  commutes with all the symmetries of  $H_1$ ,  $\tilde{C}_4^n$  and  $\tilde{C}_4^n \tilde{\sigma}_d$ ; however, it breaks  $\tilde{C}_8$  (and its odd powers). Also, importantly,  $H_W$  couples between basis states in the two blocks, so we need to treat all 16 basis states together. We therefore form a representation of  $D_8$  in  $16 \times 16$  matrices, which decomposes as  $4E_1 \oplus 4E_3$ . These two-dimensional irreducible representations imply all eigenvalues are doubly-degenerate, but the four-fold degeneracy at the Dirac point is now lifted. Since  $H_W$  preserves TRS, the bands below the gap must have total  $\mathcal{C} = 0$ .

## Appendix D: Trends with $N_a$

Having established that one approximant system with  $N_a = 3$  is topological over a wide region in parameter-space, we wish to demonstrate that this behaviour will be preserved in the quasicrystalline limit  $N_a \rightarrow \infty$ . To do so, we fix the coupling strengths at  $U/E_R = 0.15, V/E_R = 0.075$  (in the centre of the topological region), and calculate the energy gap  $\Delta E$  for increasing values of  $N_a$ . Changing  $N_a$  is simply equivalent to tuning different parameters of the Hamiltonian (the  $\tilde{\mathbf{G}}$ -vectors); provided the energy gap does not close under this tuning, the topological index of the bands below the gap cannot change.

The results are shown in Fig. 11(a). Although there is some variation due to the accuracy of different approximants to the quasicrystal (which does not necessarily improve with every step in  $N_a$ ),  $\Delta E$  shows no sign of vanishing.

This is evidence that the quasicrystal will be topological at this single point in parameter space. To go further, we investigate the extent of the topological region in parameter-space for different approximants by fixing  $U/E_R = 0.15$ , and calculating the positions  $V_{\min}$  and  $V_{\max}$  of the lower and upper boundaries of the topological region. The results are plotted in Fig. 11(b). Again, there is some variation in the plot, but we can safely conclude that there will be a wide topological region in the quasicrystalline limit.

---

[1] D. Shechtman, I. Blech, D. Gratias, and J. W. Cahn, *Physical Review Letters* **53**, 1951 (1984).

[2] R. Lifshitz, *Foundations of Physics* **33**, 1703 (2003).

[3] P. Anderson, *Physical review* **109**, 1492 (1958).

[4] E. Abrahams, P. W. Anderson, D. C. Licciardello, and T. V. Ramakrishnan, *Physical Review Letters* **42**, 673 (1979).

[5] F. Evers and A. D. Mirlin, *Reviews of Modern Physics* **80**, 1355 (2008).

[6] S. Aubry and G. André, *Annals of the Israel Physical Society* **3**, 133 (1980).

[7] G. Roati, C. D'Errico, L. Fallani, M. Fattori, C. Fort, M. Zaccanti, G. Modugno, M. Modugno, and M. Inguscio, *Nature* **453**, 895 (2008).

[8] Y. Lahini, R. Pugatch, F. Pozzi, M. Sorel, R. Morandotti, N. Davidson, and Y. Silberberg, *Physical Review Letters* **103**, 013901 (2009).

[9] J. Biddle and S. Das Sarma, *Physical Review Letters* **104**, 070601 (2010).

[10] J. Biddle, D. J. Priour, B. Wang, and S. Das Sarma, *Physical Review B* **83**, 075105 (2011).

[11] S. Ganeshan, J. Pixley, and S. Das Sarma, *Physical Review Letters* **114**, 146601 (2015).

[12] X. Li and S. Das Sarma, *Physical Review B* **101**, 064203 (2020).

[13] F. A. An, K. Padavić, E. J. Meier, S. Hegde, S. Ganeshan, J. Pixley, S. Vishveshwara, and B. Gadway, *Physical Review Letters* **126**, 040603 (2021).

[14] Y. Wang, J.-H. Zhang, Y. Li, J. Wu, W. Liu, F. Mei, Y. Hu, L. Xiao, J. Ma, C. Chin, and S. Jia, *Physical Review Letters* **129**, 103401 (2022).

[15] T. Devakul and D. A. Huse, *Physical Review B* **96**, 214201 (2017).

[16] A. Szabó and U. Schneider, *Physical Review B* **101**, 014205 (2020).

[17] E. Gottlob and U. Schneider, *Physical Review B* **107**, 144202 (2023).

[18] Z. Zhu, S. Yu, D. Johnstone, and L. Sanchez-Palencia, *Physical Review A* **109**, 013314 (2024).

[19] C. W. Duncan, *Physical Review B* **109**, 014210 (2024).

[20] R. Nandkishore and D. A. Huse, *Annual Review of Condensed Matter Physics* **6**, 15 (2015).

[21] F. Alet and N. Laflorencie, *Comptes Rendus Physique* Quantum simulation / Simulation quantique, **19**, 498 (2018).

[22] D. A. Abanin, E. Altman, I. Bloch, and M. Serbyn, *Reviews of Modern Physics* **91**, 021001 (2019).

[23] I. V. Gornyi, A. D. Mirlin, and D. G. Polyakov, *Physical Review Letters* **95**, 206603 (2005).

[24] D. M. Basko, I. L. Aleiner, and B. L. Altshuler, *Annals of Physics* **321**, 1126 (2006).

[25] V. Oganesyan and D. A. Huse, *Physical Review B* **75**, 155111 (2007).

[26] A. Pal and D. A. Huse, *Physical Review B* **82**, 174411 (2010).

[27] M. Serbyn, Z. Papić, and D. A. Abanin, *Physical Review Letters* **111**, 127201 (2013).

[28] D. A. Huse, R. Nandkishore, and V. Oganesyan, *Physical Review B* **90**, 174202 (2014).

[29] V. Ros, M. Müller, and A. Scardicchio, *Nuclear Physics B* **891**, 420 (2015).

[30] D. J. Luitz, N. Laflorencie, and F. Alet, *Physical Review B* **91**, 081103 (2015).

[31] J. Z. Imbrie, *Journal of Statistical Physics* **163**, 998 (2016).

[32] S. Iyer, V. Oganesyan, G. Refael, and D. A. Huse, *Physical Review B* **87**, 134202 (2013).

[33] X. Li, S. Ganeshan, J. Pixley, and S. Das Sarma, *Physical Review Letters* **115**, 186601 (2015).

[34] X. Li, X. Li, and S. Das Sarma, *Physical Review B* **96**, 085119 (2017).

[35] F. Setiawan, D.-L. Deng, and J. H. Pixley, *Physical Review B* **96**, 104205 (2017).

[36] V. Khemani, D. N. Sheng, and D. A. Huse, *Physical Review Letters* **119**, 075702 (2017).

[37] S.-X. Zhang and H. Yao, *Physical Review Letters* **121**, 206601 (2018).

[38] J. Smith, A. Lee, P. Richerme, B. Neyenhuis, P. W. Hess, P. Hauke, M. Heyl, D. A. Huse, and C. Monroe, *Nature Physics* **12**, 907 (2016).

[39] K. X. Wei, C. Ramanathan, and P. Cappellaro, *Physical Review Letters* **120**, 070501 (2018).

[40] M. Schreiber, S. S. Hodgman, P. Bordia, H. P. Lüschen, M. H. Fischer, R. Vosk, E. Altman, U. Schneider, and I. Bloch, *Science* **349**, 842 (2015).

[41] A. Lukin, M. Rispoli, R. Schittko, M. E. Tai, A. M.

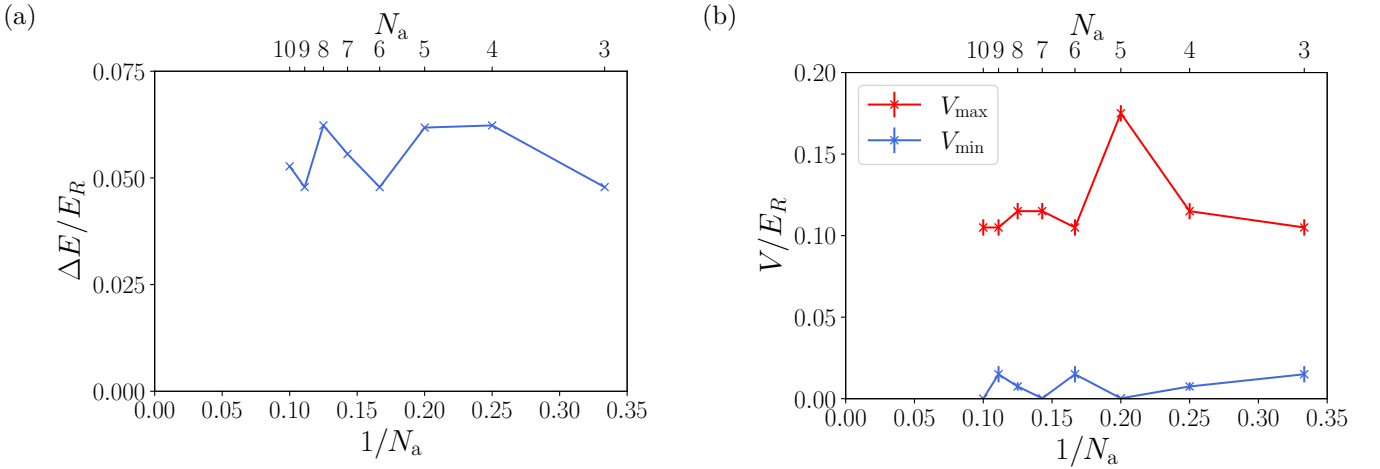


FIG. 11: (a) Energy gap for different approximant systems, for fixed  $U/E_R = 0.15, V/E_R = 0.075$ . The quasicrystalline limit is  $1/N_a \rightarrow 0$ , that is, the  $y$ -axis. (b) Upper and lower boundaries of the topological phase for different approximants, for  $U/E_R = 0.15$ . Error bars indicate the confidence interval on each value, generally  $\pm 0.005$ .

Kaufman, S., Choi, V., Khemani, J., Léonard, and M. Greiner, *Science* **364**, 256 (2019).

[42] W. De Roeck and F. Huveneers, *Physical Review B* **95**, 155129 (2017).

[43] D. J. Luitz, F. Huveneers, and W. De Roeck, *Physical Review Letters* **119**, 150602 (2017).

[44] T. Thiery, F. Huveneers, M. Müller, and W. De Roeck, *Physical Review Letters* **121**, 140601 (2018).

[45] I.-D. Potirniche, S. Banerjee, and E. Altman, *Physical Review B* **99**, 205149 (2019).

[46] A. Morningstar, L. Colmenarez, V. Khemani, D. J. Luitz, and D. A. Huse, *Physical Review B* **105**, 174205 (2022).

[47] D. Sels, *Physical Review B* **106**, L020202 (2022).

[48] J. Léonard, S. Kim, M. Rispoli, A. Lukin, R. Schittko, J. Kwan, E. Demler, D. Sels, and M. Greiner, *Nature Physics* **19**, 481 (2023).

[49] S. Kondov, W. McGehee, W. Xu, and B. DeMarco, *Physical Review Letters* **114**, 083002 (2015).

[50] J.-y. Choi, S. Hild, J. Zeiher, P. Schauß, A. Rubio-Abadal, T. Yefsah, V. Khemani, D. A. Huse, I. Bloch, and C. Gross, *Science* **352**, 1547 (2016).

[51] K. Agarwal, E. Altman, E. Demler, S. Gopalakrishnan, D. A. Huse, and M. Knap, *Annalen der Physik* **529**, 1600326 (2017).

[52] T. B. Wahl, A. Pal, and S. H. Simon, *Nature Physics* **15**, 164 (2019).

[53] S. Gopalakrishnan and D. A. Huse, *Physical Review B* **99**, 134305 (2019).

[54] H. Théveniaut, Z. Lan, G. Meyer, and F. Alet, *Physical Review Research* **2**, 033154 (2020).

[55] A. Kshetrimayum, M. Goihl, and J. Eisert, *Physical Review B* **102**, 235132 (2020).

[56] E. Chertkov, B. Villalonga, and B. K. Clark, *Physical Review Letters* **126**, 180602 (2021).

[57] D. C. W. Foo, N. Swain, P. Sengupta, G. Lemarié, and S. Adam, *Physical Review Research* **5**, L032011 (2023).

[58] S. J. Thomson and J. Eisert, *Nature Physics* **20**, 1401 (2024).

[59] P. Sierant, M. Lewenstein, A. Scardicchio, L. Vidmar, and J. Zakrzewski, *Reports on Progress in Physics* **88**, 026502 (2025).

[60] A. Štrkalj, E. V. H. Doggen, and C. Castelnovo, *Physical Review B* **106**, 184209 (2022).

[61] P. Bordia, H. Lüschen, S. Scherg, S. Gopalakrishnan, M. Knap, U. Schneider, and I. Bloch, *Physical Review X* **7**, 041047 (2017).

[62] M. Sbroscia, K. Viebahn, E. Carter, J.-C. Yu, A. Gaunt, and U. Schneider, *Physical Review Letters* **125**, 200604 (2020).

[63] J. Hur, J. Li, B. Lee, K. Kwon, M. Kim, S. Hwang, S. Kim, Y. S. Yu, A. Chan, T. Wahl, and J. yoon Choi, Stability of many-body localization in two dimensions (2025), [arXiv:2508.20699 \[cond-mat.quant-gas\]](https://arxiv.org/abs/2508.20699).

[64] J. Fan and H. Huang, *Frontiers of Physics* **17**, 13203 (2021).

[65] O. Zilberberg, *Optical Materials Express* **11**, 1143 (2021).

[66] C. W. Duncan, S. Manna, and A. E. B. Nielsen, *Physical Review B* **101**, 115413 (2020).

[67] D. Johnstone, M. J. Colbrook, A. E. B. Nielsen, P. Öhberg, and C. W. Duncan, *Physical Review B* **106**, 045149 (2022).

[68] F. Balling-Ansø, J. L. Krogh, E. E. Lassen, and A. E. B. Nielsen, Identification and Properties of Topological States in the Bulk of Quasicrystals (2025), [arXiv:2507.20722 \[quant-ph\]](https://arxiv.org/abs/2507.20722).

[69] C.-B. Hua, R. Chen, B. Zhou, and D.-H. Xu, *Physical Review B* **102**, 241102 (2020).

[70] R. Chen, C.-Z. Chen, J.-H. Gao, B. Zhou, and D.-H. Xu, *Physical Review Letters* **124**, 036803 (2020).

[71] T. Peng, C.-B. Hua, R. Chen, Z.-R. Liu, D.-H. Xu, and B. Zhou, *Physical Review B* **104**, 245302 (2021).

[72] T. Peng, Y.-C. Xiong, C.-B. Hua, Z.-R. Liu, X. Zhu, W. Cao, F. Lv, Y. Hou, B. Zhou, Z. Wang, and R. Xiong, *Physical Review B* **109**, 195301 (2024).

[73] D. Varjas, A. Lau, K. Pöyhönen, A. R. Akhmerov, D. I. Pikulin, and I. C. Fulga, *Physical Review Letters* **123**, 196401 (2019).

[74] C. Wang, F. Liu, and H. Huang, *Physical Review Letters* **129**, 056403 (2022).

[75] M. A. Bandres, M. C. Rechtsman, and M. Segev, *Phys-*

ical Review X **6**, 011016 (2016).

[76] E. Gottlob, D. S. Borgnia, R.-J. Slager, and U. Schneider, *PRX Quantum* **6**, 020359 (2025).

[77] A.-L. He, L.-R. Ding, Y. Zhou, Y.-F. Wang, and C.-D. Gong, *Physical Review B* **100**, 214109 (2019).

[78] H. Huang and F. Liu, *Physical Review Letters* **121**, 126401 (2018).

[79] Y. E. Kraus, Y. Lahini, Z. Ringel, M. Verbin, and O. Zilberberg, *Physical Review Letters* **109**, 106402 (2012).

[80] Y. E. Kraus and O. Zilberberg, *Physical Review Letters* **109**, 116404 (2012).

[81] Y. E. Kraus, Z. Ringel, and O. Zilberberg, *Physical Review Letters* **111**, 226401 (2013).

[82] T. Peng, C.-B. Hua, R. Chen, D.-H. Xu, and B. Zhou, *Physical Review B* **103**, 085307 (2021).

[83] I. Petrides, H. M. Price, and O. Zilberberg, *Physical Review B* **98**, 125431 (2018).

[84] D.-T. Tran, A. Dauphin, N. Goldman, and P. Gaspard, *Physical Review B* **91**, 085125 (2015).

[85] W. DeGottardi, D. Sen, and S. Vishveshwara, *Physical Review Letters* **110**, 146404 (2013).

[86] I. Fulga, D. Pikulin, and T. Loring, *Physical Review Letters* **116**, 257002 (2016).

[87] R. Ghadimi, T. Sugimoto, and T. Tohyama, *Journal of the Physical Society of Japan* **86**, 114707 (2017).

[88] R. Ghadimi, T. Sugimoto, K. Tanaka, and T. Tohyama, *Physical Review B* **104**, 144511 (2021).

[89] M. Tezuka and N. Kawakami, *Physical Review B* **85**, 140508 (2012).

[90] Y. Cao, Y. Zhang, Y.-B. Liu, C.-C. Liu, W.-Q. Chen, and F. Yang, *Physical Review Letters* **125**, 017002 (2020).

[91] M. Verbin, O. Zilberberg, Y. E. Kraus, Y. Lahini, and Y. Silberberg, *Physical Review Letters* **110**, 076403 (2013).

[92] M. Verbin, O. Zilberberg, Y. Lahini, Y. E. Kraus, and Y. Silberberg, *Physical Review B* **91**, 064201 (2015).

[93] Z. Che, Y. Zhang, W. Liu, M. Zhao, J. Wang, W. Zhang, F. Guan, X. Liu, W. Liu, L. Shi, and J. Zi, *Physical Review Letters* **127**, 043901 (2021).

[94] C. Gross and I. Bloch, *Science* **357**, 995 (2017).

[95] I. Bloch, J. Dalibard, and S. Nascimbène, *Nature Physics* **8**, 267 (2012).

[96] F. Schäfer, T. Fukuhara, S. Sugawa, Y. Takasu, and Y. Takahashi, *Nature Reviews Physics* **2**, 411 (2020).

[97] M. H. Anderson, J. R. Ensher, M. R. Matthews, C. E. Wieman, and E. A. Cornell, *Science* **269**, 198 (1995).

[98] K. B. Davis, M. O. Mewes, M. R. Andrews, N. J. van Druten, D. S. Durfee, D. M. Kurn, and W. Ketterle, *Physical Review Letters* **75**, 3969 (1995).

[99] M. Greiner, O. Mandel, T. Esslinger, T. W. Hänsch, and I. Bloch, *Nature* **415**, 39 (2002).

[100] M. Ben Dahan, E. Peik, J. Reichel, Y. Castin, and C. Salomon, *Physical Review Letters* **76**, 4508 (1996).

[101] O. Morsch, J. H. Müller, M. Cristiani, D. Ciampini, and E. Arimondo, *Physical Review Letters* **87**, 140402 (2001).

[102] K. Singh, K. Saha, S. A. Parameswaran, and D. M. Weld, *Physical Review A* **92**, 063426 (2015).

[103] K. Viebahn, M. Sbroscia, E. Carter, J.-C. Yu, and U. Schneider, *Physical Review Letters* **122**, 110404 (2019).

[104] L. Guidoni, C. Triché, P. Verkerk, and G. Grynberg, *Physical Review Letters* **79**, 3363 (1997).

[105] N. Cooper, J. Dalibard, and I. Spielman, *Reviews of Modern Physics* **91**, 015005 (2019).

[106] M. Aidelsburger, M. Atala, M. Lohse, J. T. Barreiro, B. Paredes, and I. Bloch, *Physical Review Letters* **111**, 185301 (2013).

[107] H. Miyake, G. A. Siviloglou, C. J. Kennedy, W. C. Burton, and W. Ketterle, *Physical Review Letters* **111**, 185302 (2013).

[108] G. Jotzu, M. Messer, R. Desbuquois, M. Lebrat, T. Uehlinger, D. Greif, and T. Esslinger, *Nature* **515**, 237 (2014).

[109] J. Léonard, S. Kim, J. Kwan, P. Segura, F. Grusdt, C. Repellin, N. Goldman, and M. Greiner, *Nature* **619**, 495 (2023).

[110] N. R. Cooper, *Physical Review Letters* **106**, 175301 (2011).

[111] N. R. Cooper and J. Dalibard, *Europhysics Letters* **95**, 66004 (2011).

[112] N. R. Cooper and R. Moessner, *Physical Review Letters* **109**, 215302 (2012).

[113] F. Wu, T. Lovorn, E. Tutuc, I. Martin, and A. H. MacDonald, *Phys. Rev. Lett.* **122**, 086402 (2019).

[114] O. E. Sommer and N. R. Cooper, *Ideal Optical Flux Lattices* (2025), arXiv:2509.01481 [cond-mat].

[115] X. Lai, G. Li, A. M. Coe, J. H. Pixley, K. Watanabe, T. Taniguchi, and E. Y. Andrei, *Nature Materials* **24**, 1019 (2025).

[116] F. D. M. Haldane, *Physical Review Letters* **61**, 2015 (1988).

[117] Numerical evaluation shows that the spatial average of the magnetic field is  $\langle B_{\text{eff}} \rangle_r \approx (1.14 \pm 0.12) \times 2\pi/\lambda^2$  (estimated by sampling different patches of the quasicrystal). However, for the periodic approximants of Sec. V, the net flux per unit cell is undefined due to points of degeneracy between spinor eigenstates.

[118] D. Jaksch and P. Zoller, *New Journal of Physics* **5**, 56 (2003).

[119] S. Spurrier and N. R. Cooper, *Physical Review A* **97**, 043603 (2018).

[120] J.-M. Gambaudo and P. Vignolo, *New Journal of Physics* **16**, 043013 (2014).

[121] T. Fukui, Y. Hatsugai, and H. Suzuki, *Journal of the Physical Society of Japan* **74**, 1674 (2005).

[122] S. Nascimbène and J. Dalibard, *Emergence of a Landau level structure in dark optical lattices* (2025), arXiv:2412.15038 [cond-mat].

[123] B. Huckestein, *Reviews of Modern Physics* **67**, 357 (1995).

[124] M. R. Zirnbauer, *Annals of Physics* **431**, 168559 (2021).

[125] E. J. Dresselhaus, B. Sbierski, and I. A. Gruzberg, *Physical Review Letters* **129**, 026801 (2022).

[126] J. Mildner, M. Caio, G. Möller, N. Cooper, and M. Bhaseen, arXiv preprint arXiv:2312.16689 (2023).

[127] B. Andrews, D. Reiss, F. Harper, and R. Roy, *Phys. Rev. B* **109**, 125132 (2024).

[128] B. Burgess, *Research data and code supporting “quasicrystalline analogue of the haldane model”* (2026).

[129] S. J. Ahn, P. Moon, T.-H. Kim, H.-W. Kim, H.-C. Shin, E. H. Kim, H. W. Cha, S.-J. Kahng, P. Kim, M. Koshino, Y.-W. Son, C.-W. Yang, and J. R. Ahn, *Science* **361**, 782 (2018).

[130] G. Yu, Z. Wu, Z. Zhan, M. I. Katsnelson, and S. Yuan, *npj Computational Materials* **5**, 1 (2019).

[131] P. Moon, M. Koshino, and Y.-W. Son, *Physical Review*

B **99**, 165430 (2019).

[132] J. A. Crosse and P. Moon, Physical Review B **103**, 045408 (2021).